Advances in high-harmonic fast wave physics in the National Spherical Torus Experiment[a)]

G. Taylor,[1,b)] R. E. Bell,[1] J. C. Hosea,[1] B. P. LeBlanc,[1] C. K. Phillips,[1] M. Podesta,[1] E. J. Valeo,[1] J. R. Wilson,[1] J-W. Ahn,[2] G. Chen,[2] D. L. Green,[2] E. F. Jaeger,[2] R. Maingi,[2] P. M. Ryan,[2] J. B. Wilgen,[2] W. W. Heidbrink,[3] D. Liu,[3] P. T. Bonoli,[4] T. Brecht,[5] M. Choi,[6] and R. W. Harvey[7]
[1]*Princeton Plasma Physics Laboratory, Princeton, New Jersey 08543, USA*
[2]*Oak Ridge National Laboratory, Oak Ridge, Tennessee 37831, USA*
[3]*University of California, Irvine, California 92697, USA*
[4]*Plasma Science and Fusion Center, MIT, Massachusetts 02139, USA*
[5]*University of Minnesota, Minnesota 55455, USA*
[6]*General Atomics, San Diego, California 92186, USA*
[7]*CompX, Del Mar, California 92014, USA*

(Received 18 November 2009; accepted 3 March 2010; published online 14 April 2010)

Improved core high-harmonic fast wave (HHFW) heating at longer wavelengths and during start-up and plasma current ramp-up has now been obtained by lowering the edge density with lithium wall conditioning, thereby moving the critical density for perpendicular fast-wave propagation away from the vessel wall. Lithium conditioning allowed significant HHFW core electron heating of deuterium neutral beam injection (NBI) fuelled H-mode plasmas to be observed for the first time. Large edge localized modes were observed immediately after the termination of rf power. Visible and infrared camera images show that fast wave interactions can deposit considerable rf energy on the outboard divertor. HHFW-generated parametric decay instabilities were observed to heat ions in the plasma edge and may be the cause for a measured drag on edge toroidal rotation during HHFW heating. A significant enhancement in neutron rate and fast-ion profile was measured in NBI-fuelled plasmas when HHFW heating was applied. © *2010 American Institute of Physics*.
[doi:10.1063/1.3371956]

I. INTRODUCTION

Many magnetically confined fusion devices rely on rf heating and current drive (CD) to provide bulk heating and to control plasma stability, including the International Thermonuclear Experimental Reactor.[1] High-harmonic fast wave (HHFW) research in the National Spherical Torus (NSTX) (Ref. 2) is directed toward maximizing the core heating and CD efficiency by reducing power loss in the plasma edge and scrapeoff layer. The electron and total heating efficiency in NSTX are determined by pulsing the rf power and then fitting the response of the electron stored energy [measured by multipoint Thomson scattering (MPTS)] and total stored energy (measured by a diamagnetic loop), respectively, with an exponential rise/fall function.[3] The CD efficiency in NSTX is determined directly by measuring the change in magnetic field pitch angle as a function of radius with a spectroscopic motional Stark effect diagnostic.[4]

HHFW experiments and modeling are motivated by the need for core heating and $q(0)$ control during noninductively sustained H-mode plasmas fuelled by energetic deuterium neutral beam injection (NBI), as well as the need to provide HHFW-driven bootstrap current during solenoid-free plasma current ramp-up.[5] Recently, considerable progress has been made in improving the HHFW coupling and heating efficiency in Ohmically heated helium and deuterium target plasmas, and in H-mode deuterium target plasmas heated and fuelled by deuterium NBI.

The 12-strap HHFW antenna in NSTX is located on the outboard midplane and extends 90° toroidally. Six decoupled 30 MHz sources can provide up to 6 MW of rf power to the antenna. The antenna launches a well-defined spectrum of directed waves with launched toroidal wavenumbers, $k_\phi = \pm 13$, ± 8, and ± 3 m^{-1}, when the phase difference ($\Delta\phi$) between adjacent antenna straps is $\pm 150°$, $\pm 90°$, and $\pm 30°$, respectively.[6,7] At other values of $\Delta\phi$ the antenna simultaneously launches several dominant spectral components. Lower k_ϕ waves should have higher CD efficiency, making $k_\phi = \pm 3$ m^{-1} particularly attractive for CD in NSTX.[3]

NSTX plasmas have a high ratio of plasma to magnetic pressure (β), typically the toroidal $\beta = 10\%-40\%$. The high β causes strong single pass absorption of HHFW by electron Landau damping and transit-time magnetic pumping,[2] even at the longest wavelengths that can be launched by the NSTX HHFW antenna (corresponding to $k_\phi = \pm 3$ m^{-1}). Both the GENRAY (Ref. 8) ray tracing and the AORSA (Ref. 9) full wave codes predict very strong first-pass absorption in the HHFW regime in NSTX[3,4] with the waves being almost entirely damped as they pass through the high β core. Consequently, rf power losses in the plasma scrapeoff and edge in the vicinity of the antenna, as opposed to multipass damping losses, play the critical role in limiting the heating efficiency in the plasma core.

There are several candidate processes that can contribute

[a)]Paper TI3 2, Bull. Am. Phys. Soc. **54**, 255 (2009).
[b)]Invited speaker.

to rf power loss near the plasma edge, including parametric decay instability (PDI) heating via ion Bernstein wave excitation,[10] and propagating and reactive wave-driven losses. The well-defined k_ϕ spectrum of the NSTX ICRF antenna allows rf coupling to be measured as a function of k_ϕ. As a result, the PDI heating and propagating fast-wave effects can be separated from surface wave interactions with the antenna and the surrounding structures. In NSTX when the edge density near the antenna is above the critical density for perpendicular fast wave propagation ($n_{\rm crit} \propto k_{ll}^2 B/\omega$, where k_{ll} is the wavevector parallel to the magnetic field, B is the magnetic field, and ω is the wave frequency) there is a reduction in core heating efficiency[3,4] which is consistent with increased surface wave propagation near the antenna and the vessel wall resulting in less rf power coupling inside the plasma separatrix. A similar behavior has been observed in conventional tokamaks at lower ICRF harmonics, where core heating efficiency is observed to be much lower with $\Delta\phi=0°$ phasing than with $\Delta\phi=180°$ phasing.[11] The mechanisms whereby rf power is lost due to surface wave propagation are not fully understood. Sheath rectification at the antenna can be enhanced due to the higher fields from the propagating modes, and far-field sheath effects can increase with decreasing k_ϕ. Also the slower group velocities and higher rf fields in the edge regions can enhance collisional damping, and rf image currents induced in the plasma will be brought closer to the antenna as the density near the antenna rises toward $n_{\rm crit}$. In summary, while it is important not to make the distance between the antenna and the location of $n_{\rm crit}$ so large that power coupling to the plasma degrades significantly, it is however also important that the edge density not be increased to the point where $n_{\rm crit}$ is so close to the antenna that surface wave interactions with the antenna and the surrounding structures may become significant.

Earlier experiments on NSTX had demonstrated improved HHFW heating efficiency in helium L-mode discharges by increasing B at the same k_ϕ.[3] Recently significant improvements in HHFW core heating efficiency were achieved by employing lithium conditioning[12] to reduce the edge density in order to move $n_{\rm crit}$ farther from the antenna and first wall.[13,14] As a result core heating at lower k_ϕ was considerably enhanced. Core electron heating and an increase in plasma stored energy were clearly observed for the first time during $k_\phi=-3$ m^{-1} rf heating of deuterium discharges. This is a particularly notable achievement because, as mentioned earlier, the CD efficiency is expected to be much higher at low k_ϕ. Lithium conditioning enabled record NSTX central electron temperatures, $T_e(0)>5$ keV in deuterium and >6 keV in helium with only ~ 3 MW of rf power at $k_\phi=-8$ m^{-1}. Lithium conditioning also resulted in the first significant core electron heating of deuterium NBI-fuelled H-mode plasmas. Most notably, coupling of rf power was maintained through the L-mode to H-mode (L-H) transition and was sustained even during H-modes with relatively large edge-localized modes (ELMs). These and other results obtained with lithium conditioning are presented in Sec. II.

Visible camera images of the antenna and visible and infrared camera images of the lower divertor region indicate that fast wave interactions can deposit considerable rf energy on the outboard divertor plate, especially for lower k_ϕ waves that begin to propagate closer to the vessel wall. Also, there is evidence that HHFW-generated PDI is heating ions in the edge and possibly driving them onto direct loss orbits that intersect the wall, and that this process may be the cause for an observed drag on toroidal rotation near the plasma edge during HHFW heating. During discharges with both HHFW and NBI heating there is an enhancement in the measured neutron rate, and fast-ion D_α (FIDA) emission diagnostic data[15] show significant enhancement and broadening of the fast-ion profile near the plasma core during HHFW heating. These observations clearly indicate a strong interaction between fast waves and fast ions. The FIDA signals have recently been compared with signals simulated by the CQL3D Fokker–Planck code[16,17] and a finite-orbit simulation by the ORBIT-RF Monte Carlo code.[18] The FIDA emission clearly shows fast-ion profile broadening that is much greater than predicted by Fokker–Planck modeling when HHFW power is applied to NBI-fuelled plasmas, pointing to the need for a full-orbit treatment in the simulation. Results on rf interactions with the plasma edge, divertor, and fast ions are presented in Sec. III.

Finally, the HHFW antenna was upgraded from a single to a double end-fed configuration. First results from this upgraded antenna show a higher arc-free power capability and are discussed in Sec. IV. A summary discussion of results and future plans is presented in Sec. V.

II. HHFW HEATING OF PLASMAS CONDITIONED WITH LITHIUM

Two lithium evaporators[12] have been used to inject collimated beams of lithium toward the lower divertor to apply lithium coatings on the graphite and carbon-fiber-composite plasma facing components in NSTX. These coatings resulted in many beneficial effects,[19] including contributing to improved HHFW electron heating in the plasma core by reducing the electron density in front of the antenna.[14] Figure 1(a) shows the significant reduction in edge density, measured by MPTS, when lithium wall conditioning is added to deuterium plasmas heated by deuterium NBI (the plasma separatrix is located at $R=1.44$ m in these discharges). The reduction in edge density produced by lithium conditioning moves $n_{\rm crit}$ away from the HHFW antenna (located at $R=1.58$ m), reducing rf power coupling near the antenna and improving coupling efficiency to the plasma core. This resulted in the production of plasmas with $T_e(0)>6$ keV in helium [Figs. 1(b) and 1(c)] and $T_e(0)>5$ keV in deuterium with only ~ 3 MW of rf power [Figs. 1(d) and 1(e)]. These temperatures are particularly impressive for NSTX which operates at a maximum axial toroidal field $B_T(0)$ of only 0.55 T. The electron temperature profile $[T_e(R)]$ became very peaked during rf heating, reaching $T_e(0)=5.2$ keV in deuterium and $T_e(0)=6.2$ keV in helium. $T_e(R)$ in deuterium is broader, with a steeper T_e gradient, probably due to the development of a reversed-shear q profile.[20,21] The helium discharge eventually transitions to an H-mode plasma late in the rf heating pulse.

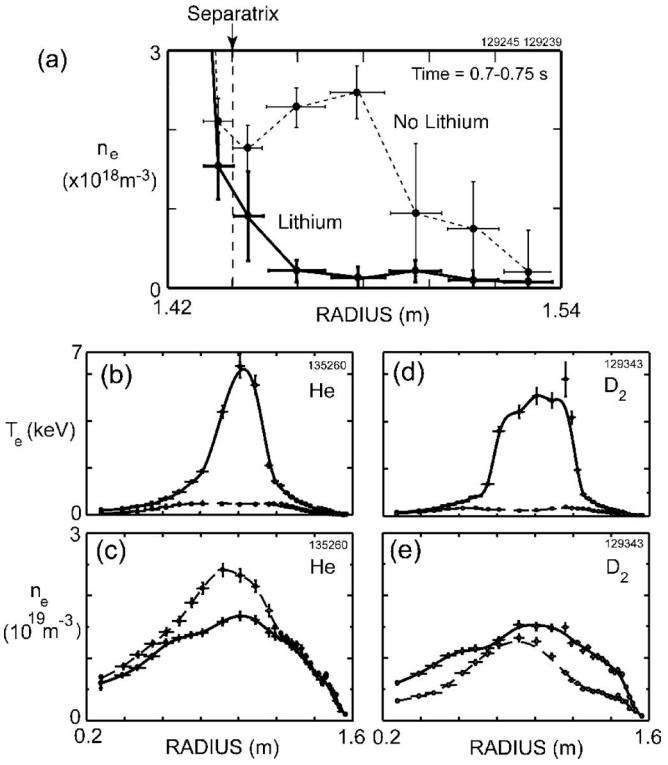

FIG. 1. (a) Time averaged MPTS $n_e(R)$ in the plasma scrapeoff between 0.7 and 0.75 s for two similar plasmas, one with lithium conditioning (shot 129254, thick error bars and solid thick line) and one without lithium conditioning (shot 129239, thin error bars and dashed line). Plasma separatrix is at $R=1.44$ m and the HHFW antenna Faraday shield is located at $R=1.58$ m. MPTS (b) $T_e(R)$ and (c) $n_e(R)$ immediately prior to rf heating (0.198 s, dashed line) and during 2.7 MW of $k_\phi=-8$ m^{-1} heating (0.298 s, solid line) of a helium plasma (shot 135260). MPTS (d) $T_e(R)$ and (e) $n_e(R)$ immediately prior to rf heating (0.148 s, dashed line) and during 3.1 MW of $k_\phi=-8$ m^{-1} heating (0.248 s, solid line) of a deuterium plasma (shot 129343).

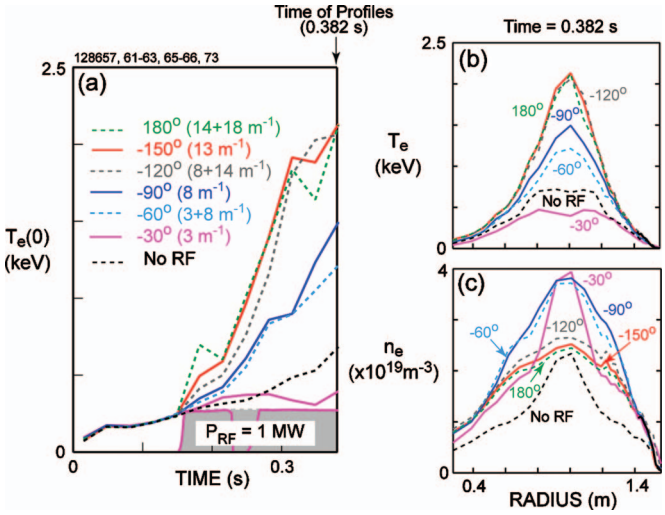

FIG. 2. (Color) (a) Time evolution of the $T_e(0)$, measured by MPTS, for a sequence of deuterium plasmas with $I_p=600$ kA, $B_T(0)=0.55$ T, 1 MW of rf power starting at 0.15 s, and no Li conditioning. $\Delta\phi$ was adjusted from $-30°$ to $180°$ in $30°$ increments between shots. $T_e(0)$ time evolution for a plasma without rf heating (black dashed line) is also plotted for comparison. Note the plasma with $\Delta\phi=-30°$ had an rf arc at 0.22 s. (b) $T_e(R)$ and (c) $n_e(R)$ measured by MPTS at 0.382 s during each discharge shown in Fig. 2(a).

A scan of $\Delta\phi$ performed for series of deuterium L-mode plasmas with $I_p=600$ kA, $B_T(0)=0.55$ T that had 1 MW of rf power starting at 0.15 s, and without using lithium conditioning, shows a degradation in heating efficiency with decreasing k_ϕ (Fig. 2) that is similar to the degradation measured in helium L-mode discharges.[4] $\Delta\phi$ was stepped from $-180°$ to $-30°$ in $30°$ increments, and included a plasma with no rf power. $T_e(0)$, measured by MPTS, [Fig. 2(a)] rises faster for larger $\Delta\phi$ (higher k_ϕ). Note for the shot with $\Delta\phi=-30°$ ($k_\phi=-3$ m^{-1}) there was an arc in the rf antenna at 0.22 s causing a notch in rf power. But even before the rf power notch it is clear the rise in $T_e(0)$ is almost the same as the shot with no rf power. Figures 2(b) and 2(c) show $T_e(R)$ and electron density profile $[n_e(R)]$ measured by MPTS at 0.382 s. Larger $\Delta\phi$ (higher k_ϕ) resulted in a more centrally peaked $T_e(R)$ and lower $\Delta\phi$ resulted in higher central electron density $[n_e(0)]$ [3]. The central electron pressure, $P_e(0)$, was about the same for shots with $|\Delta\phi|>60°$, with $P_e(0)$ in the range 8.3–9.0 kPa. $P_e(0)$ decreased significantly for $|\Delta\phi|\leq 60°$, so that $P_e(0)=7.0$ kPa at $\Delta\phi=-60°$ and $P_e(0)=2.5$ kPa at $\Delta\phi=-30°$.

Central electron heating at $k_\phi=-3$ m^{-1} in NSTX was only observed in deuterium plasmas when lithium wall conditioning was employed to reduce the edge density. Figure 3 shows the time evolution of the line-integrated electron density (n_eL) measured by MPTS, the plasma stored energy, $T_e(0)$ measured by MPTS, and the rf power for two similar deuterium L-mode plasmas with 20 mg/min of lithium wall conditioning. Shot 129679 (solid line) had up to 1.3 MW of $k_\phi=-3$ m^{-1} rf power. Shot 129677 (dashed line) had less than 150 kW of $k_\phi=-3$ m^{-1} rf power (curtailed in time by arcs). There was a clear rise in plasma stored energy and n_eL at each rf pulse in shot 129679 relative to shot 129677. However, while $T_e(0)$ increased initially it fell before the end of each rf pulse. Since the density at the antenna was still above n_{crit} in this case, the heating efficiency was still lower than at higher k_ϕ.

Lithium conditioning also enabled the first observation of significant HHFW central heating during NBI-fuelled deuterium H-mode plasmas. Earlier attempts to couple HHFW power into deuterium NBI-fuelled H-mode plasmas in NSTX, without the benefit of lithium conditioning and at lower $B_T(0)=0.45$ T, resulted in edge ion heating, but no core heating.[22] Figure 4 shows (a) $T_e(R)$, (b) $n_e(R)$, and (c) $P_e(R)$ measured by MPTS at 0.482 s for two $I_p=1$ MA, $B_T(0)=0.55$ T deuterium plasmas. One of the discharges had 2 MW of NBI and 1.6 MW of rf power, with $\Delta\phi=180°$ ($k_\phi=(14+18)$ m^{-1}), from 0.3 to 0.5 s (thick solid line, shot 129386), and the other discharge had only 2 MW of NBI (thin dashed line, shot 129381). There was a significant increase in $T_e(0)$ and $P_e(0)$ during the rf heating pulse. Shot 129386 was modeled with the TRANSP time-dependent transport analysis code.[23] The time-averaged electron thermal diffusivity was obtained for a time window that included the HHFW heating pulse. This diffusivity was then used to predict the $T_e(0)$ and $P_e(0)$ time evolution for the same shot but without HHFW heating. HHFW heating increased $T_e(0)$ and

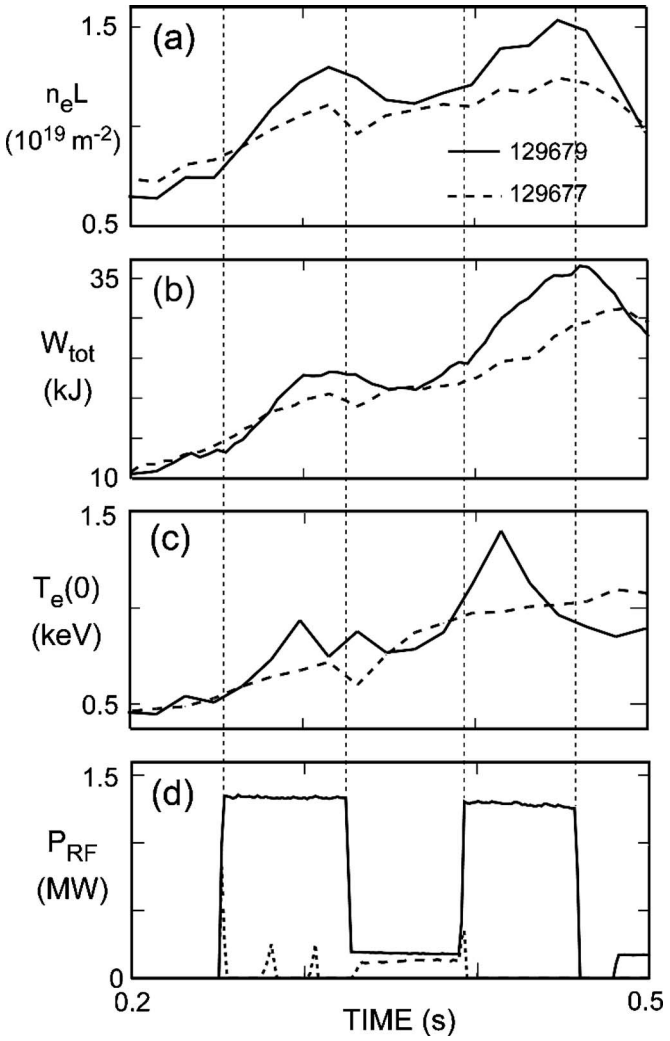

FIG. 3. Time evolution of (a) n_eL measured by MPTS, (b) plasma stored energy, (c) $T_e(0)$ measured by MPTS, and (d) rf power for two similar deuterium L-mode plasmas with 20 mg/min of lithium wall conditioning. Shot 129679 (solid line) had up to 1.3 MW of $k_\phi=-3\ m^{-1}$ rf power. Shot 129677 (dashed lines) had less than 150 kW of $k_\phi=-3\ m^{-1}$ rf power.

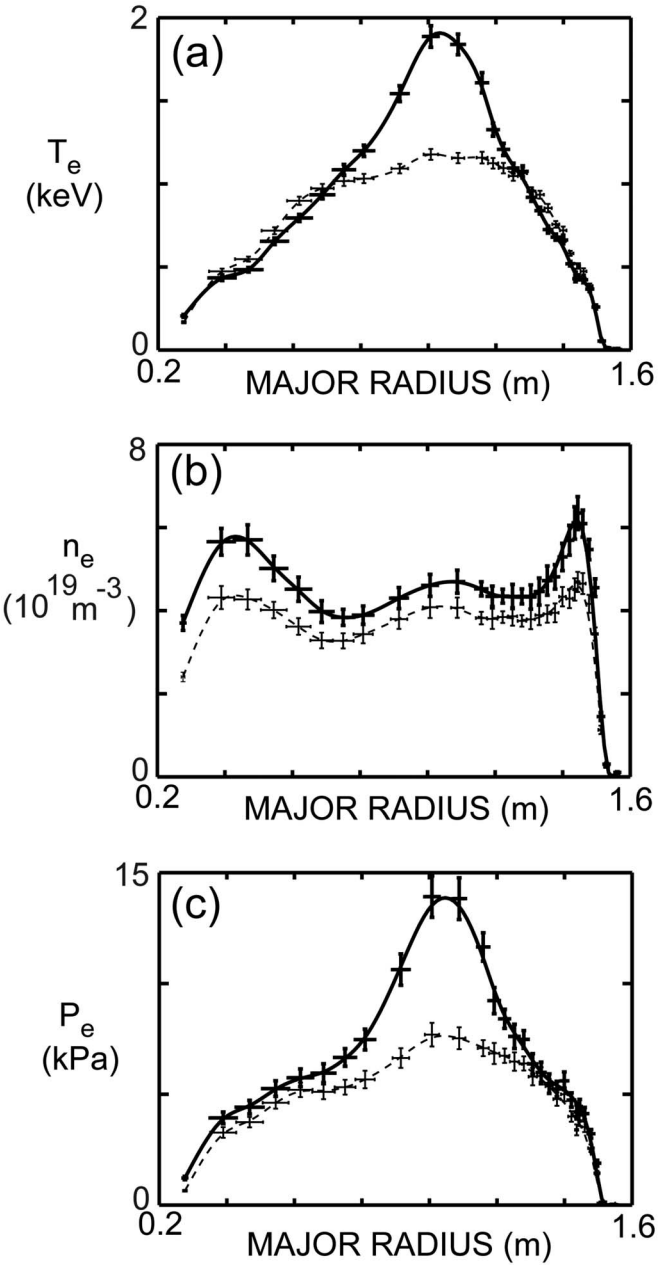

FIG. 4. (a) $T_e(R)$, (b) $n_e(R)$, and (c) $P_e(R)$ measured by MPTS at 0.482 s for two $I_p=1$ MA, $B_T(0)=0.55$ T deuterium plasmas. One discharge had 2 MW of NBI and 1.6 MW of rf power, with $\Delta\phi=180°$ ($k_\phi=(14+18)\ m^{-1}$), from 0.3 to 0.5 s (thick solid line, shot 129386), and the other discharge had 2 MW of NBI from 0.09 to 0.69 s (thin dashed line, shot 129381).

$P_e(0)$ by about 45% at the time of the profiles shown in Fig. 4. A result that is similar to the experiment.

The discharges in Fig. 4 benefited mostly from residual lithium coatings that had been laid down hours before and had minimal newly deposited lithium. H-mode plasmas heated by NBI, and conditioned with new lithium coatings that were replenished throughout the discharge, have been heated with 1.8 MW of $k_\phi=-13\ m^{-1}$ and $k_\phi=-8\ m^{-1}$ power (antenna launch spectra that can both heat and drive current). Electron heating was shifted off axis and less heating was measured at $k_\phi=-8\ m^{-1}$ than at $k_\phi=-13\ m^{-1}$, similar to the heating efficiency trend measured in L-mode plasmas.[13] About 66% of the rf power (~1.2 MW) was estimated to couple to the plasma at $k_\phi=-13\ m^{-1}$ and about 40% (~0.7 MW) was coupled at $k_\phi=-8\ m^{-1}$. MPTS edge density data indicated that the edge density was below n_{crit} for the case with $k_\phi=-13\ m^{-1}$ heating but it was above n_{crit} for the case with $k_\phi=-8\ m^{-1}$ heating.

Figure 5(a) shows the time history of the plasma stored energy for a plasma with $k_\phi=-13\ m^{-1}$ heating (shot 130608, solid black line) compared to the background plasma with no rf heating (shot 130609, dashed black line). The rf pulse on shot 130608 turned off three times, the first two times because of an antenna arc (0.375 and 0.437 s) and the third time during a programmed rf pulse shutdown (0.5 s). There was a clear rise in plasma stored energy during each rf pulse and at the end of each rf pulse there was a large type 1 ELM, indicated by the spike in divertor D_α emission (red line). Figure 5(b) shows an enlarged time window around the time of the arc at 0.375 s, the large ELM clearly followed the turn off of the rf pulse. Similarly, Fig. 5(c) shows that the large

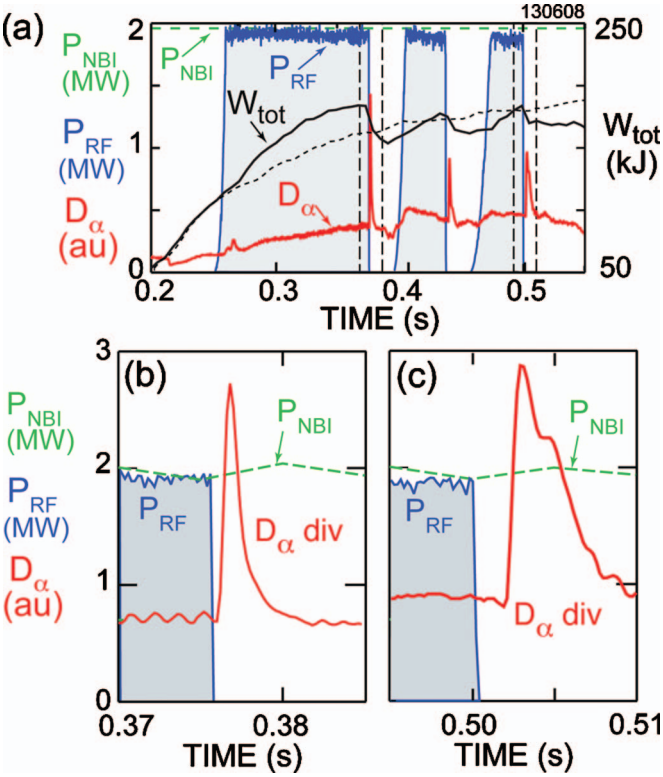

FIG. 5. (Color) (a) Time evolution of rf power (blue line), NBI power (dashed green line), plasma stored energy (solid black line), and lower divertor D_α emission (red line) during an $I_p=1$ MA, $B_T(0)=0.55$ T deuterium NBI H-mode plasma with $k_\phi=-13$ m^{-1} heating (shot 130608). The time evolution of the plasma stored energy for a similar plasma, but without rf heating (shot 130609), is shown by the dashed black line. rf power trips off during an antenna arc at 0.375 and 0.437 s, and is turned off at 0.5 s, in each case there is a large D_α spike associated with a type 1 ELM. (b) Expanded time window around the time of the arc at 0.375 s and (c) around the time of the rf turn-off at 0.5 s.

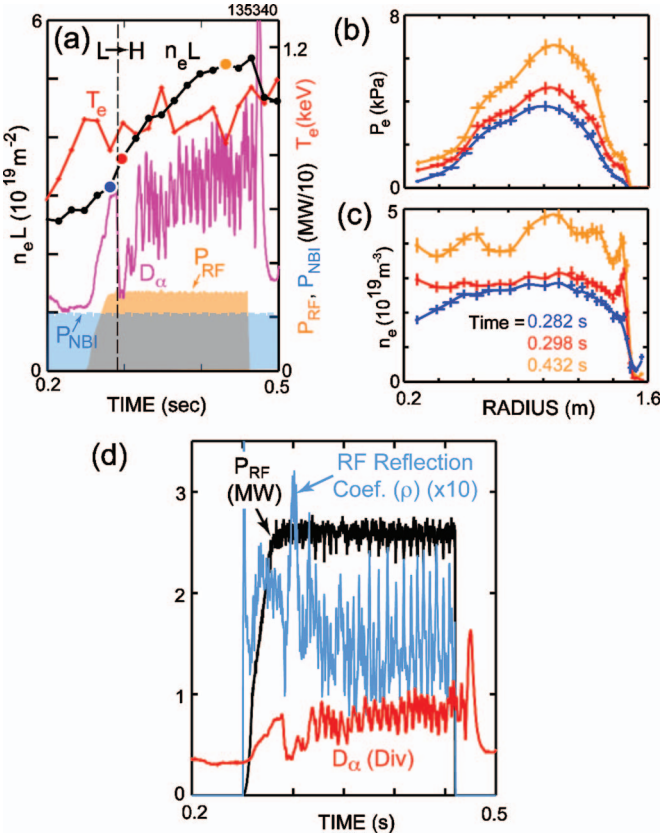

FIG. 6. (Color) (a) Time evolution of the $T_e(0)$, n_eL, rf and NBI power, and the lower divertor D_a emission during an $I_p=800$ kA, $B_T(0)=0.55$ T deuterium plasma (shot 135340) heated by 2 MW of NBI that transitions to an ELM-ing H-mode during the rf pulse at 0.29 s. This plasma had 2.7 MW of $k_\phi=-13$ m^{-1} heating from 0.25 to 0.46 s. (b) $P_e(R)$ and (c) $n_e(R)$ measured by MPTS just before (0.282 s, blue line) and after (0.298 s, red line) the L-H transition, and at the end of the rf pulse (0.432 s, orange line). (d) rf power (black line), rf voltage reflection coefficient (blue line), and lower divertor D_a emission (red line) during shot 135340.

ELM followed the shut down of the rf power. Fast camera images prior to the growth of the ELM do not show the usual helical ELM structure.[13] Thus the ELM appears to be caused by the removal of the rf power via an arc or rf pulse turnoff. As will be seen in the next section, the edge rotation clamps during HHFW heating. It is possible then that the ELM is triggered when the edge rotation increases and the edge $E_r \times B$ shear changes after the rf power is turned off.

A challenge for coupling HHFW to H-mode plasmas is to maintain good coupling through the L-H transition and large ELMs that can significantly modify the edge density profile and change the separation between the antenna and the n_{crit} location. This can in turn lead to large changes in reflected power that can exceed the rf reflection coefficient trip level (typically set to 60%–70% of the forward rf power) shutting down the rf sources. The issue here is not that 100% reflected power would damage the rf sources, but rather that there is a need to discriminate between reflections due to effects outside the antenna, and arcs in the antenna that could potentially lead to serious damage. Figure 6 shows data from an $I_p=800$ kA, $B_T(0)=0.55$ T deuterium plasma (shot 135340), conditioned with lithium, which was initially heated by 2 MW of NBI. A rf power of 2.7 MW at $k_\phi=-13$ m^{-1} was applied from 0.25 to 0.46 s and an L-H transition occurred soon after the start of the rf pulse at 0.29 s. Figure 6(a) shows the drop in divertor D_α emission at the time of the L-H transition followed by a sequence of D_α spikes during the ELMs. In this case rf power was sustained through the L-H transition and the ELMs. Figures 6(b) and 6(c) show MPTS $P_e(R)$ and $n_e(R)$ profiles at three times, just before (0.282 s) and after (0.298 s) the L-H transition and near the end of the rf pulse (0.432 s). The edge density profile rapidly steepened at the L-H transition and $P_e(0)$ doubled during the rf pulse. Figure 6(d) shows the rf voltage reflection coefficient (blue) overlaid on the rf power waveform (black) and the divertor D_α signal (red). While there were large fluctuations in the reflection coefficient, they only exceeded 0.3 briefly at the L-H transition in this case and never approached the trip level of 0.7.

Lithium wall conditioning also improved HHFW coupling during discharge start-up and early plasma current ramp-up. This is particularly important because in solenoid-free scenarios, HHFW-generated bootstrap current ramp-up to $I_p>400$ kA is needed to provide sufficient current to confine the 90 keV NBI ions in NSTX.[4] In recent experiments,

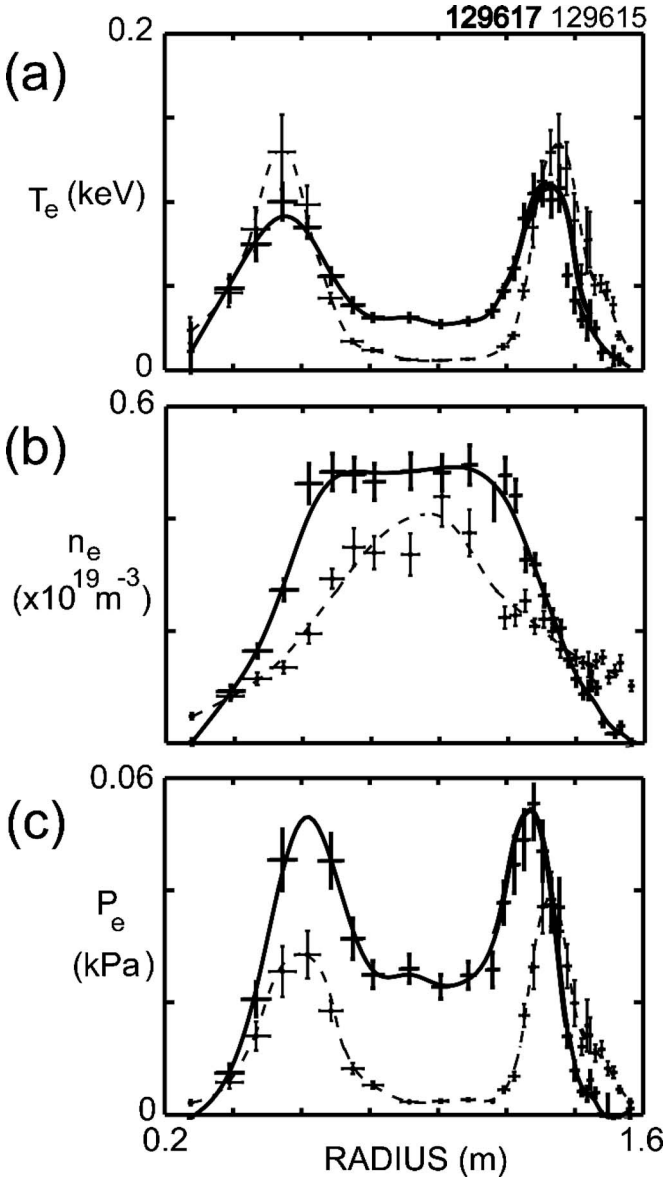

FIG. 7. (a) Electron temperature, (b) electron density, and (c) electron pressure profiles measured by MPTS for two $B_T(0)=0.55$ T deuterium plasmas at 0.052 s, during the beginning of the current ramp-up. One discharge has 550 kW of $k_\phi=-8$ m^{-1} heating coupled from 0.02 s (thick solid line) and the other discharge has no rf coupled (thin dashed line).

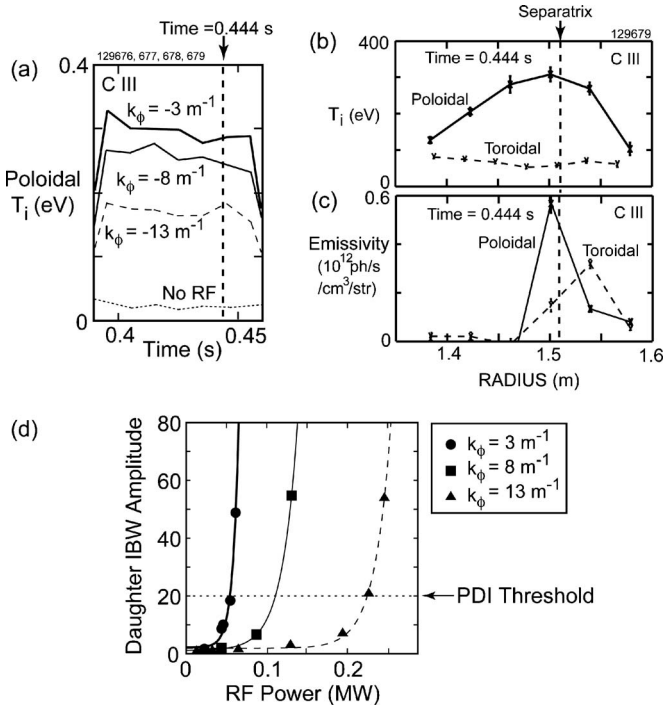

FIG. 8. Anisotropic C III ion heating measured near the plasma separatrix by passive ion spectroscopy. (a) Poloidal ion temperature at a major radius, $R=1.500$ m during 1.2–1.3 MW of $k_\phi=-3$ m^{-1} (thick solid line, shot 129679), $k_\phi=-8$ m^{-1} (thin solid line, shot 129678), $k_\phi=-13$ m^{-1} (dashed solid line, shot 129676) rf heating of $I_p=650$ kA, $B_T(0)=0.55$ T deuterium discharges. Also included is a shot with no rf power (shot 129677, dotted line). For the case with $k_\phi=-3$ m^{-1} heating at 0.444 s, radial profiles of (b) poloidal (solid line) and toroidal ion temperature (dashed line), and (c) poloidal (solid line) and toroidal (dashed line) C III emissivity. (d) Results from a one-dimensional full wave model of the PDI-generated IBW amplitude vs pump field and rf power.

$k_\phi=-8$ m^{-1} rf power has been successfully coupled into lithium-conditioned deuterium plasmas at very low $T_e(0)$ and I_p. A rf power of 550 kW was coupled between 9 and 22 ms during the initiation of a discharge by coaxial helicity injection (CHI),[24] increasing $T_e(0)$ from 3 to 15 eV when $n_e(0)$ $\sim 4\times 10^{18}$ m^{-3}. In addition, 550 kW of $k_\phi=-8$ m^{-1} power was coupled from 20 to 64 ms into the early I_p ramp following CHI. Figure 7 shows (a) $T_e(R)$, (b) $n_e(R)$, and (c) $P_e(R)$ measured by MPTS at 52 ms for a plasma with rf power (solid line) and a similar plasma without rf power (dashed line). With the addition of rf power, $T_e(0)$ increased from 3 to 33 eV, $n_e(R)$ broadened and $n_e(0)$ increased by about 20%. As a result $P_e(0)$ increased by about an order of magnitude, although $P_e(R)$ remained hollow with $P_e(R)_{\max}/P_e(0)\sim 2$.

III. RF INTERACTION WITH PLASMA EDGE, DIVERTOR, AND FAST IONS

While surface wave losses can be reduced by edge conditioning techniques, such as lithium wall coatings, there is evidence of other detrimental rf power loss processes, particularly at lower k_ϕ. Previous passive spectroscopic ion temperature measurements for helium plasmas by the edge rotation diagnostic[10] on NSTX indicated that PDI-generated ion Bernstein wave (IBW) ion heating may account for the loss of 16%–23% of the rf power through ion collisions with poorly confined edge electrons.[25] But the direct loss of PDI-generated energetic ions in the plasma edge may also be a significant loss channel for rf power. PDI-generated edge ion heating of carbon-III was measured during a sequence of similar $I_p=650$ kA, $B_T(0)=0.55$ T deuterium discharges with 1.2–1.3 MW of rf heating in which k_ϕ was changed from −13 to −3 m^{-1}. The poloidal edge ion temperature near the plasma separatrix ($R\sim 1.5$ m) was measured to increase with decreasing k_ϕ, as shown in Fig. 8(a), indicating increased rf power deposition in the edge region at lower k_ϕ. The ion heating became increasingly anisotropic as k_ϕ was reduced, with no change in toroidal ion temperature as k_ϕ was changed. Similar edge ion heating behavior was seen for C VI, He II, and Li II. The C III poloidal ion temperature [Fig. 8(b)] and emissivity peaked at the plasma separatrix,

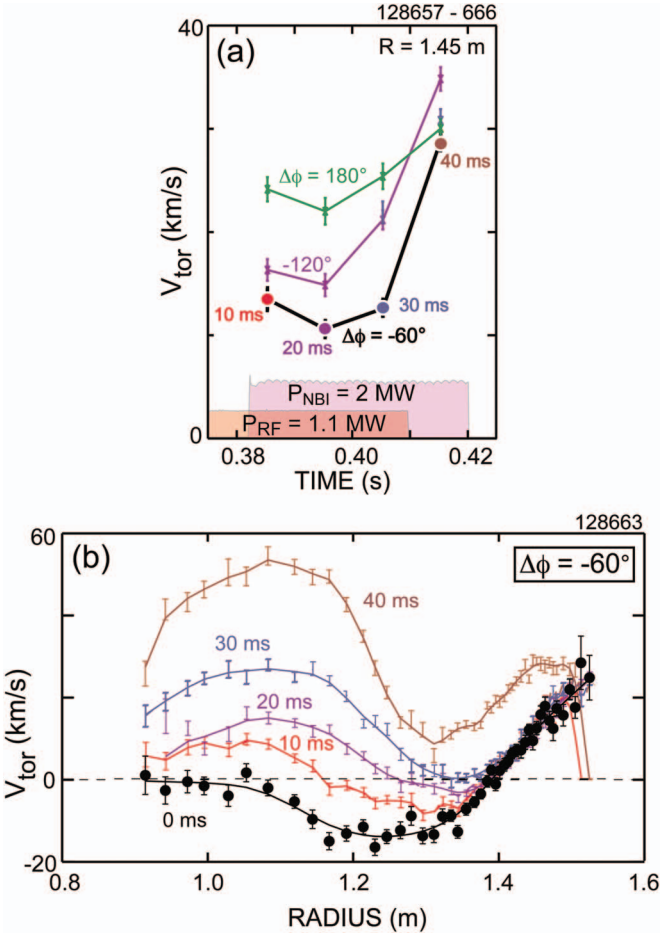

FIG. 9. (Color) (a) Toroidal velocity of C IV measured at $R=1.45$ m by CHERS during a short 2 MW NBI blip at the end of a 1.1 MW rf pulse for the $\Delta\phi=-60°$ to $-180°$ scan shown in Fig. 2. (b) Toroidal velocity of C VI vs major radius for the $\Delta\phi=-60°$ rf heating case shown in Fig. 9(a) and Fig. 2.

whereas the C III toroidal emissivity peaked outside the plasma separatrix, as shown in Fig. 8(c). A one-dimensional full wave model[26] was used to simulate the dependence of the amplitude of the PDI-generated IBW on the rf power for the range of k_ϕ values used in the experiment, and the results are summarized in Fig. 8(d). The model predicts that the threshold for PDI should fall with decreasing k_ϕ, as seen in the experiment, and that PDI should be generated with only ~100 kW of rf power at $k_\phi=3$ m^{-1} and ~250 kW at $k_\phi=13$ m^{-1}. So the rf power levels used in the experiment were well above the threshold levels expected to drive PDI.

Evidence for possible direct loss of PDI-generated energetic ions in the plasma edge is provided by charge exchange recombination spectroscopy (CHERS) (Ref. 27) measurements of the plasma toroidal rotation velocity (V_{tor}) [13]. CHERS data were measured during a 40 ms, 2 MW NBI pulse that overlapped the end of the rf heating pulse by 30 ms during the antenna $\Delta\phi$ scan shown in Fig. 2. The CHERS measurements for C VI V_{tor} at $R=1.45$ m, just inside the plasma separatrix, during the antenna $\Delta\phi$ scan are plotted in Fig. 9(a). The edge V_{tor} slowed down more at lower $\Delta\phi$ (lower k_ϕ) and after the rf power is turned off V_{tor} immediately increased. Figure 9(b) shows the C VI V_{tor} profiles measured by CHERS for the shot with $\Delta\phi=-60^0$. The profiles marked "10 ms," "20 ms," and "30 ms" are measured when the rf power was turned on. V_{tor} began to increase as the NBI imparted toroidal rotation to the core of the plasma, but V_{tor} near the edge remained clamped until the rf power was turned off, as indicated by the profile marked "40 ms." The black curve with the solid circles, marked "0 ms," is the extrapolated V_{tor} profile before the NBI pulse was turned on. There was no toroidal rotation near the axis before the NBI pulse. The sudden relatively large increase in rotation near the plasma magnetic axis when the rf power was turned off suggests that rf heating also imposed a drag on core rotation. These results support the hypothesis that ions are gaining perpendicular energy from the PDI (Ref. 10) and are then being ejected into the plasma scrapeoff, increasing the electric field and possibly changing $E_r \times B$ shear in the edge. The large ELMs observed following the turn off of rf power in HHFW+NBI H-modes, discussed in the last section, may be triggered by a change in edge $E_r \times B$ shear, but this remains to be established.

As discussed in the previous section, about a third of the $k_\phi=-13$ m^{-1} rf power is estimated to be lost before it can couple to plasma inside the separatrix of an HHFW+NBI H-mode under the discharge conditions of Fig. 5, and this loss increases to about two-thirds for $k_\phi=-8$ m^{-1} rf heating, for similar conditions. While PDI-related mechanisms may account for some of this rf power loss, it seems likely that there is a significant additional fast-wave power loss mechanism occurring in these H-mode discharges. Evidence for this mechanism is provided by visible color and infrared camera measurements, as shown in Fig. 10. Figures 10(a)–10(c) show visible color camera images taken during three $I_p=1$ MA, $B_T(0)=0.55$ T deuterium H-mode plasmas. Image (a) is from a plasma that had only 2 MW of NBI heating (shot 130609). Images (b) and (c) are from plasmas that had 2 MW of NBI heating, but also had 1.8 MW of $k_\phi=-8$ m^{-1} heating (shot 130621) and 1.9 MW $k_\phi=-13$ m^{-1} heating (shot 130608), respectively. The images in frames (b) and (c) were taken at 0.335 s. Image (a) was taken at 0.350 s. A NBI-only background frame at 0.250 s in each shot was subtracted from each image to show differences in the image when HHFW power was applied. When rf heating was applied, power flowed along the magnetic field lines onto the lower outer divertor plate. This flow became much more prominent for the case with $k_\phi=-8$ m^{-1} heating [Fig. 10(b)] than for the case with $k_\phi=-13$ m^{-1} heating [Fig. 10(c)], in keeping with lower core heating efficiency at $k_\phi=-8$ m^{-1}. Recently, dramatic evidence of the power densities associated with this interaction has been provided by calibrated infrared camera measurements of the lower divertor plates. Figure 10(d) shows a plot of the heat flux versus major radius for two, H-mode discharges, one with 2 MW of NBI (black dashed line), and one with 2 MW of NBI and 2.6 MW of $k_\phi=-8$ m^{-1} heating (red solid line). These discharges had a similar shape to the ones in Figs. 10(a)–10(c). The heat flux to the lower outer divertor plate increased by about a factor of 6 at $R=0.98$ m, to 3 MW/m^2 when rf heating was applied. Interestingly, recent 2-D AORSA modeling of NSTX HHFW plasmas, with the model boundary extended

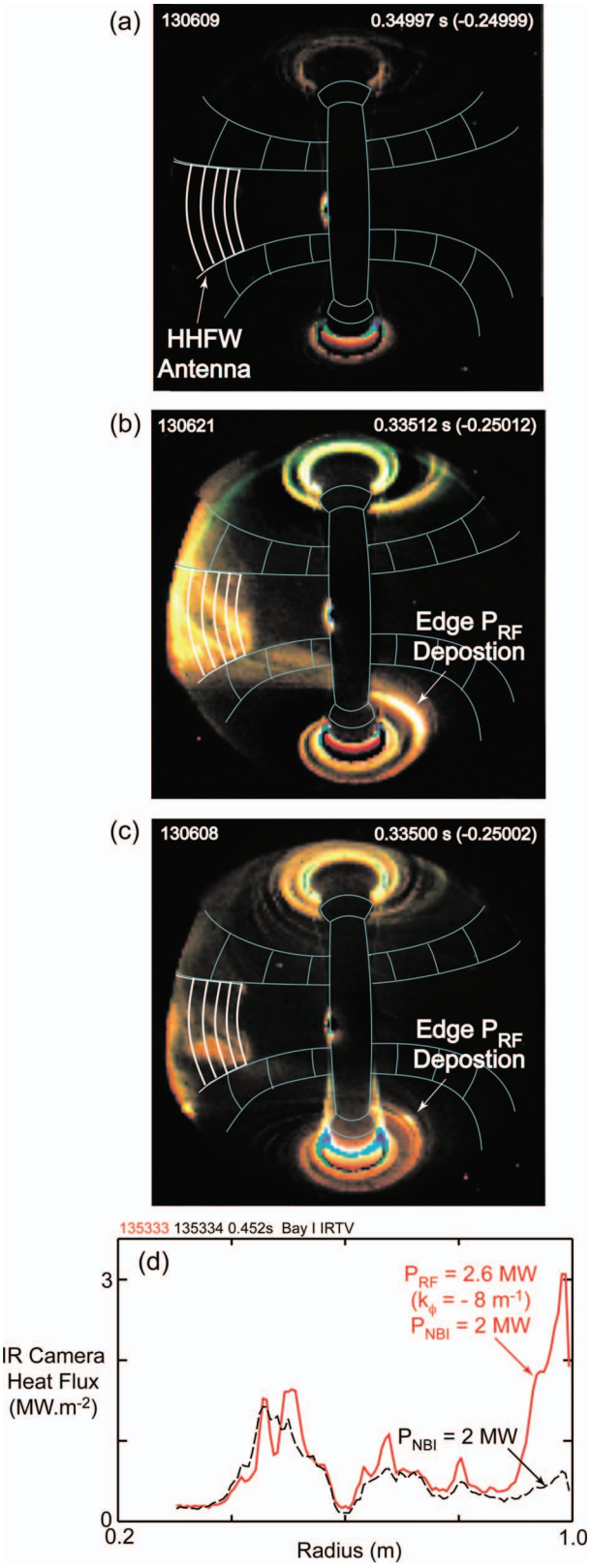

FIG. 10. (Color) Visible color camera images taken during three I_p=1 MA, $B_T(0)$=0.55 T deuterium H-mode plasmas. (a) For plasma with only 2 MW of NBI heating (shot 130609). [(b) and (c)] For plasmas with 2 MW of NBI heating and 1.8 MW of k_ϕ=−8 m^{-1} heating (shot 130621) and 1.9 MW k_ϕ=−13 m^{-1} heating (shot 130608), respectively. (d) Radial heat flux measured by an IR camera viewing the lower divertor plate during two I_p=800 kA, $B_T(0)$=0.45 T deuterium H-mode plasmas, one with 2 MW of NBI (shot 135334, dashed black line) and the other with 2 MW of NBI and 2.6 MW of k_ϕ=−8 m^{-1} heating (shot 135333, red solid line).

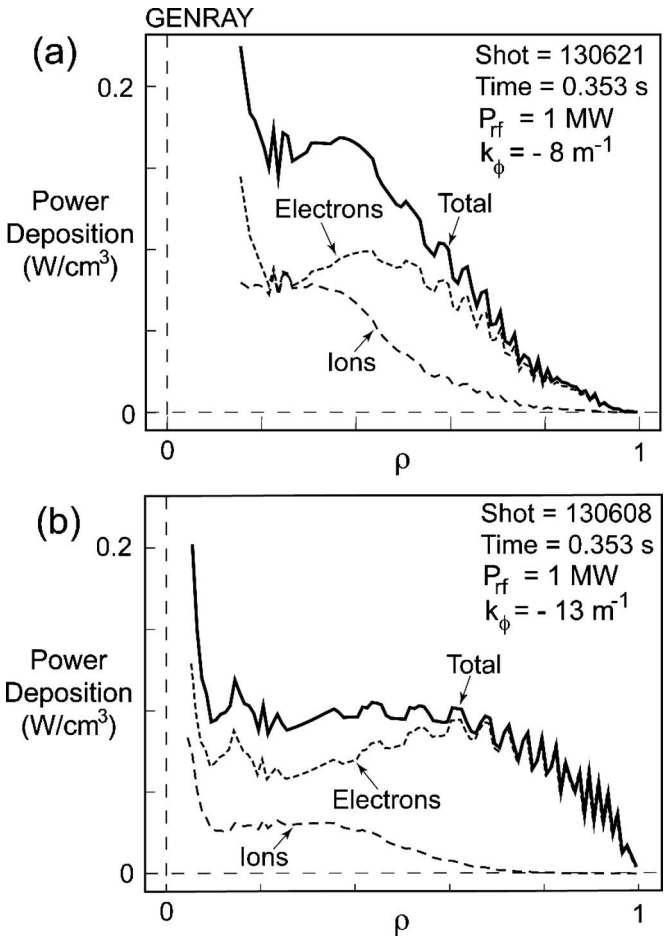

FIG. 11. Power deposition profiles calculated by GENRAY for I_p=1 MA, $B_T(0)$=0.55 T deuterium H-mode plasmas with 1 MW of (a) k_φ=−8 m^{-1} (shot 130621) and (b) k_φ=−13 m^{-1} heating (shot 130608).

outside the plasma separatrix to the vacuum vessel wall,[28] also predicts extensive rf electric fields in the scrapeoff, particularly for k_ϕ=±3 m^{-1} heating. This extended boundary modeling is now being incorporated into the three-dimensional AORSA simulation code.

GENRAY (Ref. 8) modeling of the power deposition and partitioning between ions and electrons has been performed for recent deuterium HHFW+NBI H-mode discharges in NSTX. Results of this modeling are summarized for k_ϕ=−8 m^{-1} (shot 130621) and k_ϕ=−13 m^{-1} (shot 130608) heating in Fig. 11. The modeling results shown in Fig. 11 used the density and effective temperature for slowing NBI deuterium ions obtained from a TRANSP analysis of shot 130609, which is similar to shots 130608 and 130621, but without rf heating. HHFW power turns on at 0.25 s in shots 130608 and 130621 and the GENRAY analysis is performed at 0.353 s. At that time, in the case with k_ϕ =−8 m^{-1} heating, about 70% of the rf power is deposited on electrons and 30% is deposited on fast ions [Fig. 11(a)]. In the case with k_ϕ=−13 m^{-1} heating, about 85% of the rf power is deposited on electrons and 15% is deposited on fast ions [Fig. 10(a)]. When an NBI fast-ion population is not included in the GENRAY modeling over 95% of the rf power is predicted to couple to electrons for both rf cases. It is important to note here that the GENRAY modeling does not

include rf acceleration of fast ions. A TORIC (Ref. 29) implementation in TRANSP, which also does not include a self-consistent treatment of the change in fast-ion population due to the rf acceleration of ions, shows a strong competition between electron and fast-ion damping in HHFW+NBI discharges that changes dynamically in time. A TORIC-TRANSP analysis of shot 130608 (Ref. 30) predicts half the rf power is damped on fast ions at the start of the rf pulse (0.25 s), falling to about 40% at the time of the GENRAY analysis (0.353 s) shown in Fig. 11(b), which is about a factor of 3 times higher than is predicted by GENRAY. These differences are being investigated.

Much of the rf power deposited on fast ions in the core is expected to result in scattering of the ions into the banana loss region in the outer two-thirds of the plasma, so it is important to directly measure the spatial changes in the fast-ion profile in the presence of HHFW. There have been numerous studies of the interaction between fast waves and fast ions,[31–35] however, most of these studies were performed at fundamental or low ion cyclotron harmonics. In contrast, in the NSTX HHFW regime there are a large number of deuterium ion resonances simultaneously present in the plasma. Previously HHFW acceleration of NBI fast ions was studied in NSTX with neutron counters and an E∥B neutral particle analyzer,[35] which yielded almost no data on the spatial interaction between the fast waves and the fast-ion population. With the installation of the FIDA (Ref. 15) diagnostic on NSTX, it has now been possible to measure the change in spatial distribution of fast ions during HHFW heating.[17] Figures 12(a)–12(c) show waveforms from a sequence of deuterium plasmas with 65 keV NBI blips [Fig. 11(a)]. A 1.1 MW $k_\phi=-8$ m^{-1} rf pulse is coupled from 0.15 to 0.4 s [Fig. 12(b)]. Neutron measurements showed a clear enhancement due to rf acceleration of NBI fast ions when shots with and without rf power were compared [Fig. 12(c)]. Figure 12(d) shows a plot of the FIDA signal measured between 0.29 and 0.36 s for three shots with rf (red line and symbols) and one shot with no rf (black line and symbols). The vertical green dashed lines indicate the major radial locations of the deuterium ion cyclotron resonances. There was a factor of 2 enhancement in the FIDA signal for the shots with rf power. The measured spatial profile was farther from the magnetic axis and broader than that predicted by the CQL3D Fokker–Planck code.[17] It appears that the finite Larmor radius and banana width can have a significant effect on the fast ion profile in NSTX. To test this hypothesis, simulations with the ORBIT-RF finite-orbit Monte Carlo code coupled with the full-wave code AORSA and CQL3D with first order orbit width correction are in progress.[18,36]

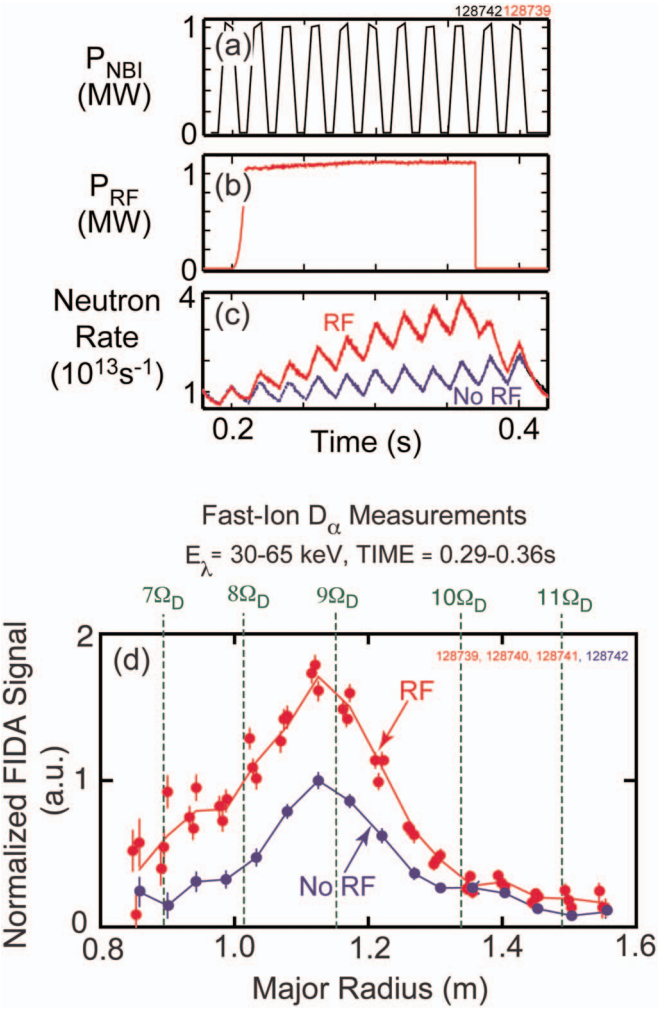

FIG. 12. (Color) (a) Time evolution of a series of short 65 keV NBI blips for two similar I_p=800 kA, $B_T(0)$=0.55 T for two similar shots 128742 and 128739. (b) $k_\phi=-8$ m^{-1} rf heating pulse for shot 128739. (c) Comparison between the measured neutron rates for shot 128739 (rf+NBI, red line) and shot 128742 (NBI, black line). (d) FIDA signal vs major radius during the time window 0.29–0.36 s for three similar plasmas with $k_\phi=-8$ m^{-1} rf heating and NBI blips (shots 128739, 128740, and 128741, red line and symbols) and a similar plasma with only NBI blips (shot 178742, blue line and symbols).

IV. RECENT RESULTS FROM THE DOUBLE END-FED ANTENNA

Until the 2009 experimental campaign, the NSTX 12-strap HHFW antenna array had been coupled to the six rf transmitters by 12 antenna feeds connected to the top of each antenna strap.[6,7] The bottom of each strap was connected to ground. Vacuum conditioning of the antenna in this configuration typically reached a system voltage limit ~25 kV, but when coupling to plasma the system voltage limit was typically <15 kV and the antenna often arced at power levels of 2–3 MW.

If the limit to the system voltage during plasma operation is set by the electric field in the vicinity of the straps and Faraday shield, then it should be possible to increase the system voltage limit during plasma operation toward the vacuum voltage limit by reducing the electric field at the straps. To accomplish this, the straps were reconfigured with a ground in the center of each strap and a transmission line was fed to both the top and bottom of each strap. This reconfiguration included installing new antenna straps and entailed adding half-wavelength loops (~5 m long) between the top and bottom antenna feeds on each strap. The total lengths of the resonant lines were adjusted so that the system voltage maxima still occurred at the five-way junction cubes. These voltage maxima are related to the magnitude of the

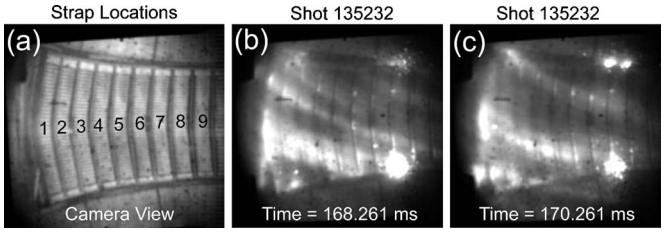

FIG. 13. Visible camera image (a) showing strap locations under uniform plasma illumination and [(b) and (c)] showing material being ejected from the antenna during plasma condition with 500 kW of rf power (enhanced online). [URL: http://dx.doi.org/10.1063/1.3371956.1]

ground currents in the straps and are not changed by the repositioning of the strap grounds. These modifications, plus increasing some critical gaps by ~20%–25%, were expected to reduce electric fields on the straps by about a factor of 2 and in the antenna box by about a factor of 1.4.

Modifications to the transmission line components external to the vacuum vessel were continued during most of the 2009 run campaign. During this time large amounts of lithium were being coated on internal vessel hardware, including the antenna hardware. The upgraded antenna was operated during the last six weeks of the campaign, and initially the system voltage limit for operation into vacuum was below 10 kV. However, the system vacuum voltages were quickly increased to their previous values of ~25 kV by dedicated vacuum conditioning. It should be noted here that 25 kV was not necessarily the maximum system voltage attainable in vacuum with the new antenna, but simply the voltage at which we chose to move on to plasma operations. Fast visible camera observations of the antenna during vacuum conditioning indicated that breakdowns were occurring in the antenna box, not in the transmission lines.

During plasma operations there was a strong correlation between antenna arcs and the ejection of lithium from the Faraday shields, and the tiles surrounding the antenna and between the straps. This behavior is consistent with the lithium on the antenna being heated by the rf sheath currents and eventually being ablated. The power and voltage limits observed in 2009 were almost certainly due to this effect. As we removed the lithium during the antenna conditioning into plasma its voltage standoff capability improved and the power coupled into plasma increased.

Figure 13 shows fast visible camera images of the antenna taken at the start of the plasma conditioning at an rf power of 500 kW that clearly show material being ejected, including lithium, from the boron nitride located between the straps and at the top and bottom of the antenna. Figure 13(a) is an image of the antenna showing strap locations under uniform plasma illumination. The camera image covers straps 1 through 9. Figures 13(b) and 13(c) show material being ejected from between straps 7 and 8 at the bottom of the antenna and from the top of the antenna between straps 7, 8, and 9. (A movie of the material ejections is available online as an enhancement to Fig. 13). While arcs in the antenna were correlated with material ejections, there were many more ejections that did not cause arcs, as in the case shown in Fig. 13. Arcs probably occur when particles enter the high rf electric field region inside the antenna Faraday shield.

When HHFW plasma operation began, 2–3 MW rf power levels were achieved more readily than during previous campaigns, and eventually exceeded the ~3 MW power level achieved in 2008. The HHFW-heated plasma performance was significantly improved over previous run campaigns. Over 4 MW was coupled into a helium L-mode plasma, $T_e(0) > 6.2$ keV was achieved with only 2.7 MW of rf power, and HHFW coupling was notably maintained through the L-H transition and during relatively large ELMs during deuterium NBI-fuelled H-mode discharges, as shown earlier in Sec. II. The improved performance and reliability of the new antenna allowed a comprehensive study of the L-H and H-L transition in helium and deuterium plasmas using only Ohmic and HHFW heating.

V. SUMMARY DISCUSSION AND FUTURE WORK

Improved core HHFW heating, particularly at longer wavelengths and during low-density start-up and plasma current ramp-up, has now been obtained by lowering the edge density with lithium wall conditioning. Significant core electron heating of NBI-fuelled H-modes has been observed for the first time over a wide range of launched wavelengths.

Visible and infrared camera images of the antenna and divertor indicate that fast wave interactions can deposit considerable rf energy on the outboard divertor plate, especially at longer wavelengths. Edge power loss was also occurring due to PDI-generated IBW that can drive ions out of the edge and onto direct loss orbits that intersect the wall, and that may be the cause for an observed drag on edge toroidal rotation in combined HHFW and NBI discharges. During plasmas where HHFW was combined with NBI, there was a significant enhancement in neutron rate and fast-ion D_α emission consistent with a strong interaction between the fast waves and the NBI fast ions. Comparison of the FIDA results with accurate physics-based modeling is essential in order to correctly interpret these data. As mentioned in Sec. III, differences between the FIDA measurements and a synthetic FIDA diagnostic[36] based on the present zero-orbit-width CQL3D Fokker–Planck and ORBIT-RF finite-orbit-width Monte Carlo simulations, support the conclusion that finite orbit-width effects need to be included in order to obtain agreement with the FIDA measurements.[37] A first order finite-orbit width correction is being added to the CQL3D code. However, fast ion orbit widths in NSTX are often comparable to the plasma width, consequently a full-finite orbit width version of CQL3D is being implemented.

Large ELMs were observed immediately following the termination of rf power, whether the power turn off was programmed or due to antenna arcing. These ELMs may be destabilized by the change in edge $E_r \times B$ shear immediately following rf power turnoff. Recently the forward and reflected power data have been digitized on some plasmas with microsecond time resolution, rather than with the usual millisecond time resolution. The time derivative of the reflection coefficient obtained from this new high time resolution data was about an order of magnitude larger for an antenna arc than for an ELM and suggests that this signal can be used to

effectively discriminate between changes in reflection coefficient due to arcs and ELMs. In 2010 the HHFW research program will use the upgraded antenna, with this ELM discrimination system, combined with a new liquid-lithium divertor,[38] to study HHFW+NBI deuterium H-modes and to develop HHFW heating of the early I_P ramp-up. HHFW system operation in 2010 will begin without a lithium coating on the antenna and antenna conditioning will be maintained throughout the campaign. This should make possible reliable operation at rf power levels up to ~5 MW.

ACKNOWLEDGMENTS

This work would not have been possible without the support of Dr. Masayuki Ono and Dr. Jonathan Menard, the NSTX team, and the machine, rf, and neutral beam operations groups.

The work is supported by the U.S. Department of Energy Contract Nos. DE-AC02-09CH11466 and DE-AC05-00OR2272.

[1] D. W. Swain and R. H. Goulding, Fusion Eng. Des. **82**, 603 (2007).
[2] M. Ono, M. G. Bell, R. E. Bell, T. Bigelow, M. Bitter, W. Blanchard, D. S. Darrow, E. D. Fredrickson, D. A. Gates, L. R. Grisham, J. C. Hosea, D. W. Johnson, R. Kaita, S. M. Kaye, S. Kubota, H. W. Kugel, B. P. LeBlanc, R. Maingi, R. Maqueda, E. Mazzucato, J. Menard, D. Mueller, B. A. Nelson, C. Neumeyer, F. Paoletti, S. F. Paul, Y.-K. M. Peng, S. Ramakrishnan, R. Raman, P. M. Ryan, S. A. Sabbagh, C. H. Skinner, T. Stevenson, D. Stutman, D. W. Swain, E. J. Synakowski, G. Taylor, A. Von Halle, J. Wilgen, M. Williams, J. R. Wilson, S. J. Zweben, R. Ackers, R. E. Barry, A. Bers, J. M. Bialek, P. T. Bonoli, M. D. Carter, J. Chrzanowski, W. Davis, E. J. Doyle, L. Dudek, P. C. Efthimion, R. Ellis, J. R. Ferron, M. Finkenthal, E. Fredd, T. Gibney, R. J. Goldston, R. E. Hatcher, R. J. Hawryluk, H. Hayashiya, K. W. Hill, T. R. Jarboe, S. C. Jardin, H. Ji, M. Kalish, P. LaMarche, L. L. Lao, K. C. Lee, F. M. Levinton, N. C. Luhmann, R. Majeski, J. Manickam, R. Marsala, T. K. Mau, B. McCormack, S. S. Medley, M. M. Menon, O. Mitarai, M. Nagata, N. Nishino, G. Oliaro, H. K. Park, R. Parsells, G. Pearson, T. Peebles, C. K. Phillips, R. Pinsker, G. D. Porter, A. K. Ram, J. Robinson, P. Roney, A. L. Roquemore, A. Rosenberg, M. Schaffer, S. Shiraiwa, P. Sichta, D. Stotler, B. C. Stratton, Y. Takase, W. R. Wampler, G. A. Wurden, X. Q. Xu, J. G. Yang, L. Zeng, and W. Zhu, Nucl. Fusion **41**, 1435 (2001).
[3] J. Hosea, R. E. Bell, B. P. LeBlanc, C. K. Phillips, G. Taylor, E. Valeo, J. R. Wilson, E. F. Jaeger, P. M. Ryan, J. Wilgen, H. Yuh, F. Levinton, S. Sabbagh, K. Tritz, J. Parker, P. T. Bonoli, R. Harvey, and NSTX Team, Phys. Plasmas **15**, 056104 (2008).
[4] C. K. Phillips, R. E. Bell, L. A. Berry, P. T. Bonoli, R. W. Harvey, J. C. Hosea, E. F. Jaeger, B. P. LeBlanc, P. M. Ryan, G. Taylor, E. J. Valeo, J. B. Wilgen, J. R. Wilson, J. C. Wright, H. Yuh, and NSTX Team, Nucl. Fusion **49**, 075015 (2009).
[5] M. Ono, Phys. Plasmas **2**, 4075 (1995).
[6] P. M. Ryan, A. L. Rosenberg, D. W. Swain, J. R. Wilson, D. B. Batchelor, M. G. Bell, R. E. Bell, S. Bernabei, J. M. Bitter, P. T. Bonoli, M. Brambilla, A. Cardinali, M. D. Carter, D. Darrow, E. Fredericksson, D. Gates, J. C. Hosea, E. F. Jaeger, S. M. Kaye, B. P. LeBlanc, R. Maingi, T. K. Mau, S. S. Medley, J. E. Menard, D. Mueller, M. Ono, F. Paoletti, Y-K. M. Peng, C. K. Phillips, R. I. Pinsker, D. A. Rasmussen, S. A. Sabbagh, E. J. Synakowski, J. B. Wilgen, and NSTX Team, in *Proceedings of the 19th IAEA Fusion Energy Conference*, Lyon, 2002, edited by M. Spak (IAEA, Vienna, 2003), Paper No. EX/P2-13.
[7] P. M. Ryan, R. E. Bell, L. A. Berry, P. T. Bonoli, R. W. Harvey, J. C. Hosea, E. F. Jaeger, B. P. LeBlanc, C. K. Phillips, G. Taylor, E. J. Valeo, J. B. Wilgen, J. R. Wilson, J. C. Wright, H. Yuh, and NSTX Team, in *Proceedings of the 35th EPS Conference on Plasma Physics*, Hersonissos, 2008, Europhysics Conference Abstracts Vol. 32D, edited by P. Lalousis (EPS, Brussels, 2008), Paper No. P-1.108.
[8] A. P. Smirnov and R. W. Harvey, Bull. Am. Phys. Soc. **40**, 1837 (1995).
[9] E. F. Jaeger, L. A. Berry, E. D'Azevedo, D. B. Batchelor, and M. D. Carter, Phys. Plasmas **8**, 1573 (2001).
[10] T. M. Biewer, R. E. Bell, S. J. Diem, C. K. Phillips, J. R. Wilson, and P. M. Ryan, Phys. Plasmas **12**, 056108 (2005).
[11] P. Colestock, G. J. Greene, J. C. Hosea, C. K. Phillips, J. E. Stevens, M. Ono, J. R. Wilson, D. A. D'Ippolito, J. R. Myra, and I. S. Lehrman, Fusion Eng. Des. **12**, 43 (1990).
[12] H. W. Kugel, D. Mansfield, R. Maingi, M. G. Bell, R. E. Bell, J. P. Allain, D. Gates, S. Gerhardt, R. Kaita, J. Kallman, S. Kaye, B. LeBlanc, R. Majeski, J. Menarda, D. Mueller, M. Ono, S. Paul, R. Raman, A. L. Roquemore, P. W. Ross, S. Sabbagh, H. Schneider, C. H. Skinner, V. Soukhanovskii, T. Stevenson, J. Timberlake, W. R. Wampler, J. Wilgren, L. Zakharov, and NSTX Team, J. Nucl. Mater. **390**, 1000 (2009).
[13] J. C. Hosea, R. E. Bell, E. Feibush, R. W. Harvey, E. F. Jaeger, B. P. LeBlanc, R. Maing, C. K. Phillips, L. Roquemore, P. M. Ryan, G. Taylor, K. Tritz, E. J. Valeo, J. Wilgen, J. R. Wilson, and NSTX Team, AIP Conf. Proc. **1187**, 105 (2009).
[14] G. Taylor, R. E. Bell, R. W. Harvey, J. C. Hosea, E. F. Jaeger, B. P. LeBlanc, C. K. Phillips, P. M. Ryan, E. J. Valeo, J. B. Wilgen, J. R. Wilson, and NSTX Team, AIP Conf. Proc. **1187**, 113 (2009).
[15] M. Podestà, W. Heidbrink, R. Bell, and R. Feder, Rev. Sci. Instrum. **79**, 10E521 (2008).
[16] R. W. Harvey and M. G. McCoy, *Proc. of IAEA Tech. Committee on Advances in Simulation and Modeling of Thermonuclear Plasmas*, Montreal, Quebec (IAEA, Vienna, 1993), p. 489, USDOC NTIS Doc. No. DE93002962.
[17] D. Liu, W. W. Heidbrink, M. Podestà, R. E. Bell, E. D. Fredrickson, S. S. Medley, R. W. Harvey, J. Hosea, and E. Ruskov, Plasma Phys. Controlled Fusion **52**, 025006 (2010).
[18] M. Choi, V. S. Chan, R. I. Pinsker, S. C. Chiu, and W. W. Heidbrink, Phys. Plasmas **12**, 072505 (2005).
[19] M. G. Bell, H. W. Kugel, R. Kaita, L. E. Zakharov, H. Schneider, B. P. LeBlanc, D. Mansfield, R. E. Bell, R. Maingi, S. Ding, S. M. Kaye, S. F. Paul, S. P. Gerhardt, J. M. Canik, J. C. Hosea, G. Taylor, and NSTX Research Team, Plasma Phys. Controlled Fusion **51**, 124054 (2009).
[20] H. Y. Yuh, F. M. Levinton, R. E. Bell, J. C. Hosea, S. M. Kaye, B. P. LeBlanc, E. Mazzucato, J. L. Peterson, D. R. Smith, J. Candy, R. E. Waltz, C. W. Domier, N. C. Luhmann, Jr., W. Lee, and H. K. Park, Phys. Plasmas **16**, 056120 (2009).
[21] E. Mazzucato, R. E. Bell, S. Ethier, J. C. Hosea, S. M. Kaye, B. P. LeBlanc, W. W. Lee, P. M. Ryan, D. R. Smith, W. X. Wang, J. R. Wilson, and H. Yuh, Nucl. Fusion **49**, 055001 (2009).
[22] B. P. LeBlanc, R. E. Bell, S. Bernabei, T. M. Biewer, J. C. Hosea, and J. R. Wilson, AIP Conf. Proc. **787**, 86 (2005).
[23] R. J. Hawryluk, in *Physics of Plasmas Close to Thermonuclear Conditions*, Proc. of the International School of Plasma Physics Vol. 1, edited by B. Coppi, G. Leotta, D. Pfirsch, R. Pozzoli, and E. Sindoni (Pergamon, Varenna, Italy, 1981), p. 19.
[24] R. Raman, T. R. Jarboe, D. Mueller, B. A. Nelson, M. G. Bell, R. Bell, D. Gates, S. Gerhardt, J. Hosea, R. Kaita, H. Kugel, B. LeBlanc, R. Maingi, R. Maqueda, J. Menard, M. Nagata, M. Ono, S. Paul, L. Roquemore, S. Sabbagh, V. Soukhanovskii, and G. Taylor, Nucl. Fusion **49**, 065006 (2009).
[25] J. R. Wilson, S. Bernabei, T. Biewer, S. Diem, J. Hosea, B. LeBlanc, C. K. Phillips, P. Ryan, and D. W. Swain, AIP Conf. Proc. **787**, 66 (2005).
[26] G. Chen, F. E. Jaeger, L. A. Berry, and J. R. Myra, Bull. Am. Phys. Soc. **54**, 71 (2009).
[27] R. E. Bell, Rev. Sci. Instrum. **77**, 10E902 (2006).
[28] D. L. Green, F. E. Jaeger, L. A. Berry, and M. Choi, Bull. Am. Phys. Soc. **54**, 70 (2009).
[29] M. Brambilla, Plasma Phys. Controlled Fusion **44**, 2423 (2002).
[30] B. P. LeBlanc, R. E. Bell, P. Bonoli, J. C. Hosea, E. Mazzucato, C. K. Phillips, A. L. Roquemore, P. M. Ryan, G. Taylor, J. R. Wilson, and H. Yuh, AIP Conf. Proc. **1187**, 117 (2009).
[31] W. W. Heidbrink and G. J. Sadler, Nucl. Fusion **34**, 535 (1994).
[32] M. Nemoto, Y. Kusama, V. I. Afanassiev, K. Hamamatsu, H. Kimura, T. Fujii, S. Moriyama, and M. Saigusa, Plasma Phys. Controlled Fusion **39**, 1599 (1997).
[33] W. W. Heidbrink, E. D. Fredrickson, T. K. Mau, C. C. Petty, R. I. Pinsker, M. Porkolab, and B. W. Rice, Nucl. Fusion **39**, 1369 (1999).
[34] M. J. Mantsinen, M.-L. Mayoral, V. G. Kiptily, S. E. Sharapov, B. Alper, A. Bickley, M. de Baar, L.-G. Eriksson, A. Gondhalekar, T. Hellsten, K. Lawson, F. Nguyen, J.-M. Noterdaeme, E. Righi, A. A. Tuccillo, and M. Zerbini, Phys. Rev. Lett. **88**, 105002 (2002).
[35] A. L. Rosenberg, J. E. Menard, J. R. Wilson, S. S. Medley, R. Andre, C.

K. Phillips, D. S. Darrow, B. P. LeBlanc, M. H. Redi, N. J. Fisch, R. W. Harvey, T. K. Mau, E. F. Jaeger, P. M. Ryan, D. W. Swain, S. A. Sabbagh, J. Egedal, and NSTX Team, Phys. Plasmas **11**, 2441 (2004).
[36]W. W. Heidbrink, E. Ruskov, E. D. Fredrickson, N. Gorelenkov, S. S. Medley, H. L. Berk, and R. W. Harvey, Plasma Phys. Controlled Fusion **48**, 1347 (2006).
[37]M. Choi, V. S. Chan, L. L. Lao, R. I. Pinsker, D. Green, L. A. Berry, F. Jaeger, J. M. Park, W. W. Heidbrink, D. Liu, M. Podesta, R. Harvey, P. Bonoli, D. N. Smithe, RF SciDAC Team, and SWIM Team, Phys. Plasmas **17**, 056102 (2010).
[38]H. W. Kugel, M. G. Bell, J.-W. Ahn, J. P. Allain, R. Bell, J. Boedo, C. Bush, D. Gates, T. Gray, S. Kaye, R. Kaita, B. LeBlanc, R. Maingi, R. Majeski, D. Mansfield, J. Menard, D. Mueller, M. Ono, S. Paul, R. Raman, A. L. Roquemore, P. W. Ross, S. Sabbagh, H. Schneider, C. H. Skinner, V. Soukhanovskii, T. Stevenson, J. Timberlake, W. R. Wampler, and L. Zakharov, Phys. Plasmas **15**, 056118 (2008).